Publication Year	2023
Acceptance in OA	2025-02-25T14:52:23Z
Title	Gaia Data Release 3. Analysis of RVS spectra using the General Stellar Parametriser from spectroscopy
Authors	Recio-Blanco, A., de Laverny, P., Palicio, P. A., Kordopatis, G., Álvarez, M. A., Schultheis, M., Contursi, G., Zhao, H., Torralba Elipe, G., Ordenovic, C., Manteiga, M., Dafonte, C., Oreshina-Slezak, I., Bijaoui, A., Frémat, Y., Seabroke, G., Pailler, F., Spitoni, E., POGGIO, Eloisa, Creevey, O. L., Abreu Aramburu, A., Accart, S., Andrae, R., Bailer-Jones, C. A. L., Bellas-Velidis, I., Brouillet, N., BRUGALETTA, Elisa, Burlacu, A., Carballo, R., Casamiquela, L., Chiavassa, A., Cooper, W. J., Dapergolas, A., Delchambre, L., Dharmawardena, T. E., DRIMMEL, Ronald, Edvardsson, B., Fouesneau, M., Garabato, D., García-Lario, P., García-Torres, M., Gavel, A., Gomez, A., González-Santamaría, I., Hatzidimitriou, D., Heiter, U., Jean-Antoine Piccolo, A., Kontizas, M., Korn, A. J., LANZAFAME, Alessandro, Lebreton, Y., Le Fustec, Y., Licata, E. L., Lindstrøm, H. E. P., Livanou, E., Lobel, A., Lorca, A., Magdaleno Romeo, A., Marocco, F., Marshall, D. J., Mary, N., Nicolas, C., Pallas-Quintela, L., Panem, C., Pichon, B., Riclet, F., Robin, C., Rybizki, J., Santoveña, R., Silvelo, A., SMART, Richard Laurence, Sarro, L. M., SORDO, Rosanna, Soubiran, C., Süveges, M., Ulla, A., VALLENARI, Antonella, Zorec, J., Utrilla, E., Bakker, J.
Publisher's version (DOI)	10.1051/0004-6361/202243750
Handle	http://hdl.handle.net/20.500.12386/36218
Journal	ASTRONOMY & ASTROPHYSICS
Volume	674

Table 3. Polynomial coefficients for the calibration of the Matisse-Gauguin gravities and metallicities.

Parameter	p_0	p_1	p_2	p_3	p_4
$\log(g)$	0.4496	−0.0036	−0.0224		
[M/H]	0.274	−0.1373	−0.0050	0.0048	
$[M/H]_{OC}$	−0.7541	1.8108	−1.1779	0.2809	−0.0222

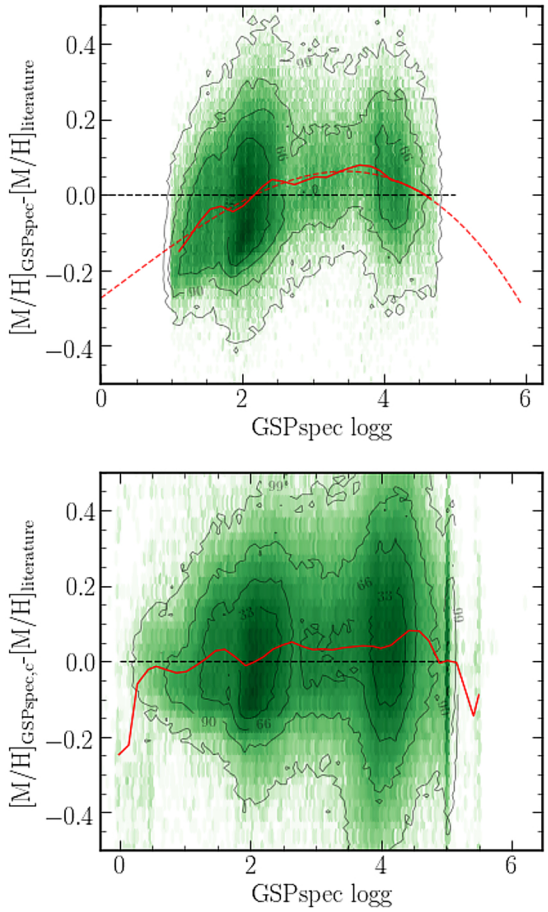

Fig. 12. Comparison of GSP-Spec and literature metallicities. *Top*: 2D histogram of the differences between the GSP-Spec metallicities and the literature values as a function of uncalibrated $\log(g)$ for our best-quality sample. The red full line is the running mean of the difference, and the dashed line is the fit to the running mean, defining the correction to apply. *Bottom*: medium-quality sample showing the differences between the calibrated metallicities and the literature values.

that we relax to smaller than or equal to three (medium quality sample, plotted in grey, $\sim 3.7 \times 10^5$ stars).

For our best quality sample, we find a median offset for $T_{\rm eff}$, $\log(g)$, [M/H] of −17 K, −0.3 dex and 0.0 dex, respectively, and a robust standard deviation (i.e. ∼1.48 times the median absolute deviation) of 90 K, 0.19 dex, and 0.13 dex. These trends are globally similar when taking into account each reference catalogue separately (see Appendix D).

Whereas $T_{\rm eff}$ and [M/H] are globally well recovered (however, see next paragraph), $\log(g)$ determination is slightly biased. GSP-Spec MatisseGauguin finds consistently lower gravities, the offset being larger for giants than for dwarfs. Based on these findings, we suggest the following calibration for $\log(g)$:

$$\log(g)_{\rm calibrated} = \log(g) + \sum_{i=0}^{2} p_i \cdot \log(g)^i. \quad (1)$$

The p_i coefficients were obtained by fitting the trends with respect to the above-mentioned literature compilation, and are reported in the first row of Table 3.

Furthermore, we note that despite finding, overall, a zero offset in metallicity, a further investigation of the trends compared to the literature shows that giants ($\log(g) \lesssim 1.5$) have slightly underestimated metallicities, whereas dwarfs ($\log(g) \gtrsim 4$) have slightly overestimated values (see top plot of Fig. 12). These trends can be corrected by fitting a low-order polynomial to the residuals as a function of *uncalibrated* $\log(g)$, and correcting the raw metallicities by this polynomial. The correction takes the form of:

$$[M/H]_{\rm calibrated} = [M/H] + \sum_{i=0}^{\rm deg} p_i \cdot \log(g)^i. \quad (2)$$

The p_i coefficients are provided in Table 3. Two different corrections are proposed. The first one, a third-order polynomial, was obtained by fitting the trends with respect to the above-mentioned literature compilation. The result of this calibration is illustrated in the bottom plot of Fig. 12. The second proposed correction, a fourth-order polynomial, is based on a set of open cluster stars with known metallicity from the literature and high membership probability (Cantat-Gaudin et al. 2020; Castro-Ginard et al. 2022; Tarricq et al. 2021). The advantage of open cluster data is that they ensure a constant metallicity at all $\log(g)$ values for the same object. However, as open clusters are thin-disc objects, the considered [M/H] range is restricted to the metal-rich regime. This alternative correction is illustrated in Fig. 13 and reported in the last row of Table 3.

9.1.2. Analysis of [α/Fe] and individual chemical abundances

To evaluate, calibrate, and remove possible gravity dependencies on the measured [α/Fe], [Fe I/H], [Fe II/H], and [X/Fe] abundance values (with X being an arbitrary element), we follow the strategy described below. It assumes that the abundance distribution (expressed relative to the solar values) should be close to zero in the solar neighbourhood for stars with metallicities close to solar and velocities close to the Local Standard of Rest (to avoid stars with large eccentricities). This strategy furthermore has the advantage of avoiding any calibration based on external catalogues. The procedure that we carry out is the following.

We first select only stars that have their first 13 quality flags (see Table 2) less or equal to one, except for their *KMgiantPar* flag and *extrapol* flag which we set to be equal to zero. In addition, we also impose that the abundance flag associated with the upper limit (*XUpLim*) is equal to zero, whereas the one associated with the uncertainties (*XUncer*) is set to less than or equal to one. Finally, we set an upper limit for their uncertainty (defined as the difference between the upper value and the lower value divided by two) and the line scatter to be less than 0.2 dex for both.

Amongst the selected stars, we further select the ones that are located within 0.25 kpc of the Sun; have a global metallicity [M/H]= 0.0 ± 0.25 dex (to avoid possible effects due to metallicty zero-point offsets); and have an azimuthal velocity V_ϕ close

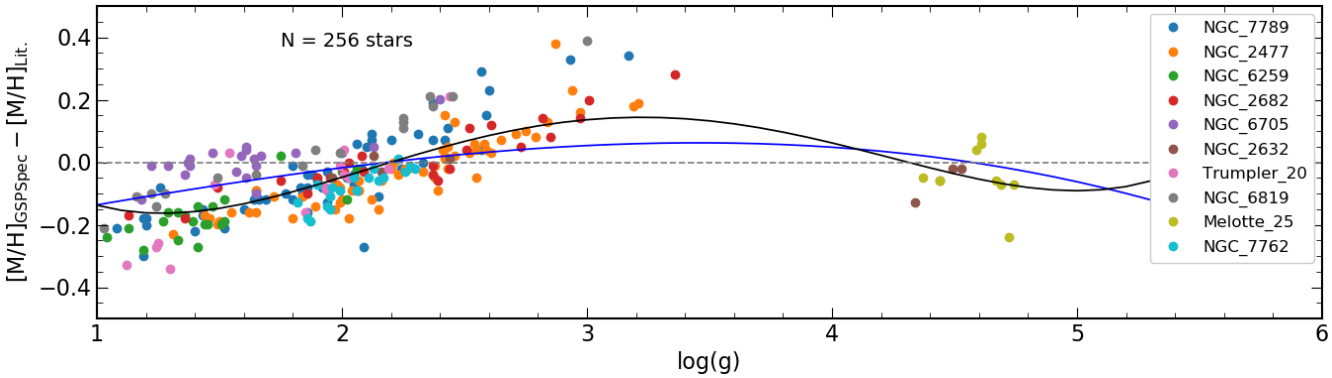

Fig. 13. Metallicity bias with respect to the literature as a function of log(g) for the open cluster stars, excluding dwarfs with S/N lower than 50. The colour code used for each cluster is indicated in the legend. The solid blue line corresponds to the general metallicity correction while the black line refers to that specifically obtained from the open clusters.

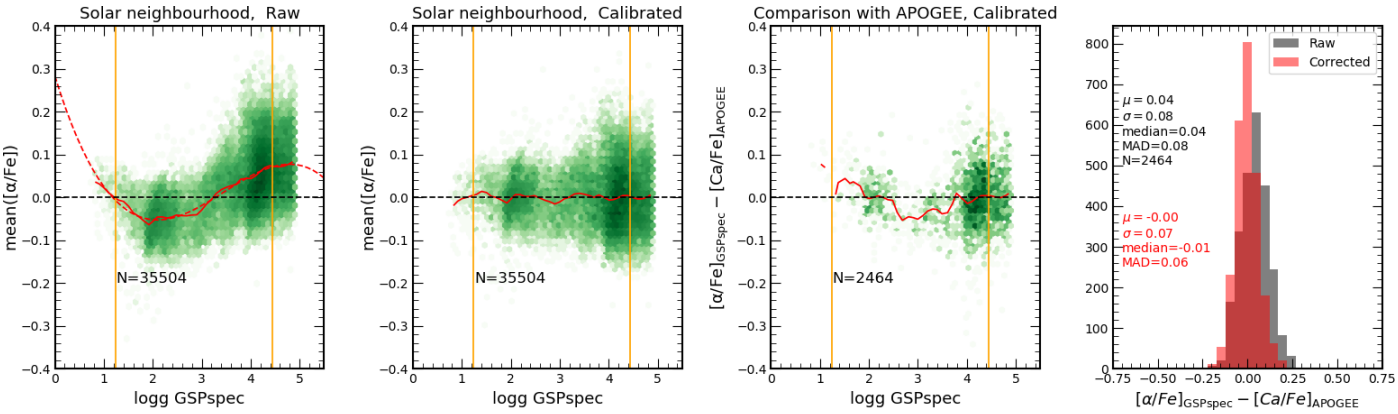

Fig. 14. Correction of [α/Fe] trends as a function of log(g). *Left panel*: the 2D histogram of the stars with 3750 K $\leq T_{\rm eff} <$ 5750 K, log(g)$<$ 4.9 in green, with all of their quality flags equal to zero, located at the solar neighbourhood, with velocities close to the LSR and metallicities close to solar values in the raw (i.e. uncalibrated) [α/Fe]-log(g) space, colour-coded by log(N). The running mean is plotted as a full red line, and its fit is the red dashed line. The dashed black line is included as a visual reference for the y-axis. Vertical orange lines indicate the log(g) range over which the calibration is assumed to be reliable (differences between the fit and the running mean smaller than 0.05 dex). The second panel is similar to the left one, but the calibration has now been applied. *Third panel*: the difference between the calibrated [α/Fe] and the calcium values from APOGEE DR17 as a function of MatisseGauguin log(g), where we have relaxed the *extrapol* flag to be less than or equal to one. Finally, the right panel shows the histograms of the differences compared to the literature data before (in grey) and after (in red) the calibration. Quantifications of the mean, median, standard deviation, and robust standard deviation (1.4826· MAD) are shown in the *top left corner* for the uncalibrated values (in grey) and in the *bottom right corner* for the calibrated values (in red).

to the Local Standard of Rest ($V_{\rm LSR} \pm 25\,{\rm km\,s^{-1}}$)[17]. By choosing such a sample, we ensure that we select stars with a high probability of having, on average, similar chemical properties to the Sun. Therefore, their $[X_1/X_2]$ abundance distributions (with X_1 and X_2 associated with two different elements or families of elements) are expected to be centred on zero.

We then compute the running mean of $[X_1/X_2]$ as a function of log(g), in bins of δlog(g)= 0.2 dex (red full line on the first row of plots in Figs. 14, E.1, and E.2). This trend, for an unbiased abundance estimation, should be centred on zero, regardless of the dispersion of the underlying distribution (which is a manifestation of either a true Galactic dispersion, or of the precision of GSP-Spec, or both).

Finally, we fit the trend defined by the running mean with a third- or fourth-order polynomial (choosing the correct compromise, depending on the data behaviour, to avoid overfittings), where each point has a weight inversely proportional to the dispersion of $[X_1/X_2]$ within the considered log(g)-bin. This fit defines the correction that could be applied to our data (red dashed line on the leftmost panels in Figs. 14, E.1, and E.2). The correction takes the form of:

$$[X_1/X_2]_{\rm calibrated} = [X_1/X_2] + \sum_{i=0}^{\rm deg} p_i \cdot \log(g)^i, \quad (3)$$

where deg = 3 or 4 and X_2 is either Fe or H, depending on the chemical species (see Table 4).

We also define the log(g) range over which the calibration is expected to be valid (vertical orange lines in the figures). The latter is evaluated by estimating the difference between the running mean and the fit, $\Delta_{\rm fit}$, and excluding the points at log(g) $\pm$ 0.4 from the boundaries for which $\Delta_{\rm fit}$ is larger than 0.05 dex (chosen arbitrarily). We note that the application of the calibration outside this log(g) confidence range should be used with caution, if not avoided. To increase the validity log(g) range for the abundances with high number statistics ([α/Fe] and [Ca/Fe]), we propose another calibration by relaxing the GSP-Spec quality flag associated to the extrapolation ($\leq$1). This leads to an alternative fourth-order polynomial fitting (second and third last rows of Table 4) and allows a qualitative view of how the correction

[17] Velocities are computed as in Gaia Collaboration (2023a).

Table 4. Polynomial coefficients, recommended parameter intervals, and *extrapol* flag values for Matisse-Gauguin [α/Fe] and individual abundance calibrations (Eq. (3)).

Element	p_0	p_1	p_2	p_3	p_4	Recommended interval		*extrapol* flag
	As a function of log(g)					Min log(g)	Max log(g)	
[α/Fe]	−0.5809	0.7018	−0.2402	0.0239	0.0000	1.01	4.85	0
[Ca/Fe]	−0.6250	0.7558	−0.2581	0.0256	0.0000	1.01	4.85	0
[Mg/Fe]	−0.7244	0.3779	−0.0421	−0.0038	0.0000	1.30	4.38	0
[S/Fe]	−17.6080	12.3239	−2.8595	0.2192	0.0000	3.38	4.81	0
[Si/Fe]	−0.3491	0.3757	−0.1051	0.0092	0.0000	1.28	4.85	0
[Ti/Fe]	−0.2656	0.4551	−0.1901	0.0209	0.0000	1.01	4.39	0
[Cr/Fe]	−0.0769	−0.1299	0.1009	−0.0200	0.0000	1.01	4.45	0
[Fe I/H]	0.3699	−0.0680	0.0028	−0.0004	0.0000	1.01	4.85	0
[Fe II/H]	35.5994	−27.9179	7.1822	−0.6086	0.0000	3.53	4.82	0
[Ni/Fe]	−0.2902	0.4066	−0.1313	0.0105	0.0000	1.41	4.81	0
[N/Fe]	0.0975	−0.0293	0.0238	−0.0071	0.0000	1.21	4.79	0
[α/Fe]	−0.2838	0.3713	−0.1236	0.0106	0.0002	0.84	4.44	≤1
[Ca/Fe]	−0.3128	0.3587	−0.0816	−0.0066	0.0020	0.84	4.98	≤1
	As a function of $t = T_{\rm eff}/5750$					Min $T_{\rm eff}$	Max $T_{\rm eff}$	
[α/Fe]	−6.6960	20.8770	−21.0976	6.8313	0.0000	4000	6830	≤1
[Ca/Fe]	−7.4577	23.2759	−23.6621	7.7657	0.0000	4000	6830	≤1
[S/Fe]	0.1930	−0.2234	0.0000	0.0000	0.0000	5700	6800	≤1

Notes. The uncertainties associated with these coefficients are provided in Table E.1.

behaves outside the log(g)-confidence range of the third-order polynomial.

We then verify on the same sample that the correction improves the trends (second column of plots of Figs. 14, E.1, and E.2).

Finally, we use literature data, which contain a wider variety of metallicities, to verify that the calibration is indeed improving the offsets (third and fourth columns of Figs. 14, E.1, and E.2). The literature data we use in this case are composed of APOGEE-DR17 and GALAH-DR3 for all of the elements except sulphur, and AMBRE for this latter abundance (Perdigon et al. 2021). In the case of [α/Fe], the comparison is made with respect to literature [Ca/Fe] values, as in the RVS domain the [α/Fe] indicators are dominated by the CaT lines. We note that, for these abundance comparisons, no agreement was required between GSP-Spec and the literature in the related stellar atmospheric parameters or the assumed solar abundances.

It can be seen from Fig. 14, E.1, and E.2 that the provided calibrations for the [α/Fe] and individual chemical abundance offsets significantly decrease their gravity dependence (and even remove it completely for several species), and that they set them close to the solar values. Moreover, the comparison with literature data is also improved, reducing the offset and/or the dispersion. The values of the polynomial coefficients of Eq. (3) (p_i) together with their domain of validity in log(g), to avoid extrapolations, are listed in Table 4. We also provide the uncertainties on the polynomial coefficients (derived from the fit) in Table E.1, as a possible criterion to evaluate the robustness of the calibration. We note that, for some elements, a lower order polynomial might be sufficient to fit the data, but the verification made on the datasets suggests that we nevertheless correct without overfitting with a third-order polynomial.

Interestingly, the methodology described above does not allow calibration of the Zr and Nd abundances, as as insufficient number of stars are selected with the criteria previously described. Furthermore, we note that the distribution of the literature [Nd/Fe] values (GALAH-DR3, Buder et al. 2021) found for our solar neighborhood sample does not peak at 0 dex; therefore, an offset correction of [Nd/Fe] would be meaningless. For the same reason, we do not apply any correction to the GSP-Spec [Ce/Fe] abundances since our cross-match with literature (Hinkel et al. 2014; Abdurro'uf et al. 2022; Forsberg et al. 2019; Buder et al. 2021) reveals a similar offset in the cerium distribution with respect to the solar value. It is also important to note that the log(g) domain covered by the abundances of these three heavy elements is not very large, minimising gravity trends in the results.

Finally, it could be convenient for some scientific purposes to calibrate the abundance trends as a function of the effective temperature instead of the gravity. This is particularly the case when hot dwarf stars are included in the used sample. For this reason, we provide an example of this alternative calibration applied to [α/Fe] and illustrated in Fig. 15. The derived third-order polynomial is provided at the end of Table 4. In those cases, the log(g) variable in Eq. (3) should be replaced by the effective temperature. The use of similar calibrations as a function of $T_{\rm eff}$ for other chemical abundances or to correct gravity trends has to be evaluated by the user, depending on the target sample and scientific goals. Such calibrations are not provided here for clarity.

9.1.3. Summary of GSP-Spec MatisseGauguin biases and proposed solutions

In this section, we summarise the observed MatisseGauguin parameter and abundance biases, as well as the recommended solutions.

Effective temperature: No significant biases are observed in $T_{\rm eff}$. For hot stars, rotational mismatches could nevertheless affect the results.

Proposed solution: The *vbroadT* flag (or the vbroad value) has to be checked and/or used to clean the samples.

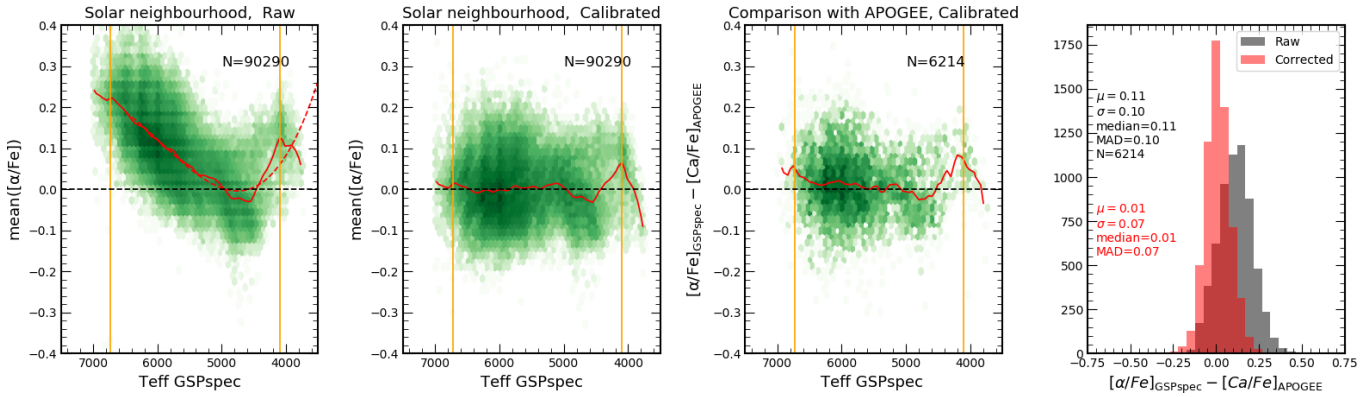

Fig. 15. Same as Fig. 14 but using the effective temperature as a reference parameter, instead of log(g). The associated polynomial coefficients and applicability intervals are provided in Table 3.

Surface gravity: A bias in log(g) is present. The median value is 0.3 dex on the entire parameter space. It shows a slight trend with $T_{\rm eff}$, getting worse as $T_{\rm eff}$ decreases. This could be related to the progressive dominance of the CaT lines as log(g) indicators (they become stronger along the giant branch as $T_{\rm eff}$ decreases), and to the absence of Paschen lines for $T_{\rm eff} \lesssim 5500$ K. No clear relation with line broadening mismatches seems to exist.

Proposed solution: A global correction is proposed based on literature data. For dwarf stars, a correction based on $T_{\rm eff}$ could offer more precise corrections, as the $T_{\rm eff}$ range is higher than the log(g) one. We generally advise to optimise the correction to the parameter space of the user.

Global metallicity: The observed log(g) bias seems to be associated with a slight [M/H] bias, presenting a similar behaviour with $T_{\rm eff}$ for $T_{\rm eff} \lesssim 5500$ K (not related to line broadening mismatches). For hotter stars, rotational mismatches could also cause a bias.

Proposed solution: Global corrections are proposed based on literature data of (i) field stars and (ii) open clusters. These corrections are only significant for giant stars in the low-log(g) regime. For hot stars, the *vbroadM* flag (or the vbroad value) has to be checked and/or used to clean the sample.

[α/Fe] and individual abundances: Atmospheric parameter biases are linked to abundance biases. In the GSP-Spec MatisseGauguin case, the main sources seem to be the log(g) bias and the rotational mismatch. On the contrary, the impact of the observed slight metallicity biases is probably reduced thanks to the fact that most abundances are derived with respect to iron. In the regime $T_{\rm eff} \lesssim 5500$ K, [α/Fe] and individual abundance biases are of small amplitude and show a very weak trend with $T_{\rm eff}$ and/or log(g). In the regime $T_{\rm eff} \gtrsim 5500$ K, abundance biases seem dominated by rotational missmatches.

Proposed solution: Global corrections are proposed as a function of log(g), based on a zero-point calibration to the Local Standard of Rest at solar metallicity. Alternatively, global corrections as a function of $T_{\rm eff}$ can be implemented (as in that proposed for [α/Fe]), with very similar results in the regime of $T_{\rm eff} \lesssim 5500$ K. For samples with a short $T_{\rm eff}$ and log(g) coverage, a constant shift to the solar value at [M/H] = 0 can be implemented if the user prefers to work with raw parameters (although the proposed calibrations are still valid). For dwarf stars, when including the hot temperature regime, a correction as a function of $T_{\rm eff}$ should be implemented. Alternatively, the sample can be cleaned using the *vbroadT*, *vbroadG,* and *vbroadM* (or the vbroad value). We generally advise optimisation of the correction to the parameter space of the user.

9.2. GSP-Spec ANN biases

The ANN workflow produces an alternative estimation of the stellar atmospheric parameters ($T_{\rm eff}$, log(g), [M/H], and [α/Fe]) that can be found in the *AstrophysicalParametersSupp* table. In the following, the observed ANN biases with respect to the literature are presented, proceeding in a similar way to that described for MatisseGauguin results (cf. Sect. 9.1.1).

Figure 16 shows the comparison with the literature for two ANN subsamples: the best quality, in green, and the medium quality, in grey. For our best-quality sample, we selected all the sources with the first eight flags equal to zero, excluding those with broadening and radial velocity issues, higher noise uncertainties, or extrapolations. The median offsets for the 274 592 stars of the best-quality sample are −114 K, −0.12 dex, and −0.24 dex for $T_{\rm eff}$, log(g), and [M/H], respectively, and the corresponding mean absolute deviations are 142 K, 0.28 dex, and 0.14 dex.

Compared to the literature, ANN results present a larger bias than MatisseGauguin in $T_{\rm eff}$ and [M/H], and a slightly lower bias in log(g). Nevertheless, these differences come partially from the fact that the ANN quality flags select a different reference subsample for the comparison statistics than the one used for GSP-Spec-MatisseGauguin. In particular, cooler giants are outside the ANN high-quality selection. Finally, the dispersion for the ANN parameterisation is also higher than for MatisseGauguin, particularly for $T_{\rm eff}$ and log(g).

We propose simple polynomial calibrations for $T_{\rm eff}$, log(g), and [M/H] based on the above comparison with the literature using the *best*-quality sample. It is important to note that the $T_{\rm eff}$ calibration of ANN is S/N dependent (cf. Appendix F) because the ANN algorithm was trained with synthetic spectra in five S/N levels (cf. Sect. 7).

We focus in the following on the high-S/N regime ($S/N_{\rm ANN} > 50$ corresponding to $S/N > 108$, cf. Table 1). For lower S/N values, we refer the reader to Appendix F, where the correct S/N optimisation of the algorithm is validated. We also highlight that, as the number of stars with $T_{\rm eff} > 6000$ K in the literature is small, the proposed corrections should not be applied beyond this temperature limit. The resulting calibrations take the form of:

$$X_{\rm calibrated} = X + \sum_{i=0}^{\rm deg} p_i \cdot X^i, \quad (4)$$

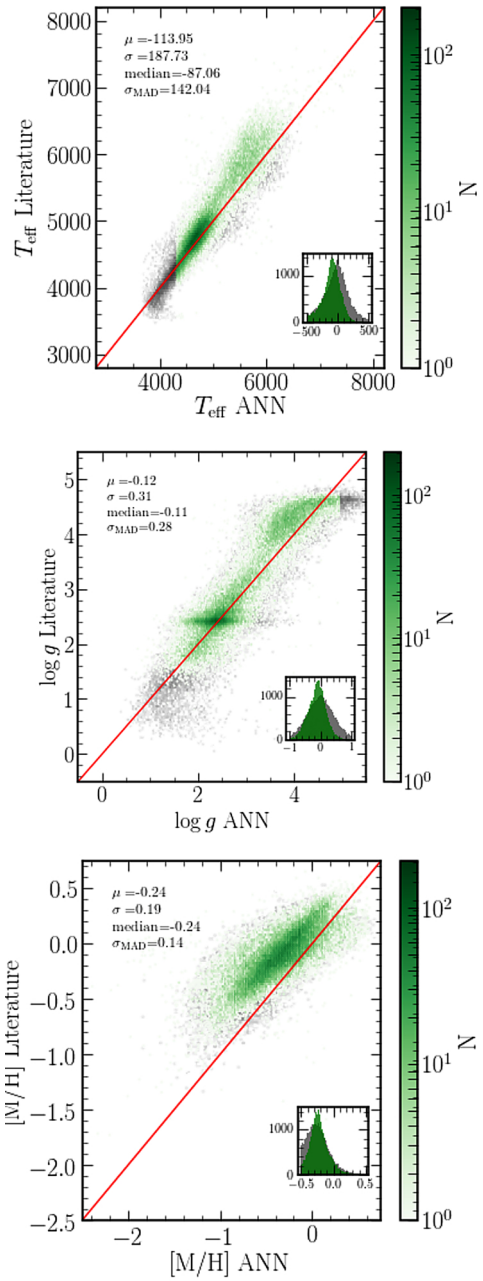

Fig. 16. Same as Fig. 11 but for GSP-Spec-ANN, published in the complementary table *AstrophysicalParametersSupp*. The reference high-quality subsample used for the comparison statistics is different from that shown in Fig. 11 (for GSP-Spec-MatisseGauguin), as imposed by the ANN quality flags.

where p_i coefficients for each parameter calibration can be found in Table 5. Moreover, similarly to MatisseGauguin results, we also suggest a calibration for [α/Fe], independent of literature data:

$$[\alpha/\mathrm{Fe}]_{\mathrm{calibrated}} = [\alpha/\mathrm{Fe}] + \sum_{i=0}^{3} p_i \cdot \log(g)^i. \quad (5)$$

In summary, although ANN parameters present slightly higher biases and uncertainties than MatisseGauguin ones (and they are therefore published in the complementary table AstrophysicalParametersSupp), their overall quality provides a methodologically different parametrisation, which could be useful, in particular, to test the MatisseGauguin classification in the low-S/N regime.

Table 5. Polynomial coefficients for the calibration of ANN parameters (at $S/N_{ANN} \sim 50$ for T_{eff}, see Appendix F for other S/N_{ANN} values).

Parameter	p_0	p_1	p_2	p_3
T_{eff}	12816	−8.1	1.65E−3	−1.07E−7
log(g)	−0.006	0.023		
[M/H]	0.092	−0.446	−0.07	
[α/Fe]	−0.038	0.099	−0.052	0.006

10. Illustration of GSP-Spec results

Illustrating all DR3 GSP-Spec results is obviously out of the scope of this paper. Two performance demonstration articles exclusively based on GSP-Spec MatisseGauguin parameters show their detailed application to Galactic chemo-dynamical studies of the disc and halo populations (Gaia Collaboration 2022a), and interstellar medium studies through the RVS diffuse interstellar band carrier (Gaia Collaboration 2022b). The homogeneous GSP-Spec treatment of the exhaustive all-sky RVS survey enables a chemo-physical parametrisation quality comparable to that of ground-based surveys of higher spectral resolution and wavelength coverage. Examples of this are the precision in the estimated individual chemical abundances (including heavy elements) allowing chemo-dynamical studies of Galactic stellar populations, DIB parameter estimation from individual spectra, and the precision in the atmospheric parameters providing clear constraints on stellar evolution models (see below).

In the following, we provide a few more examples of GSP-Spec results, focusing on (i) the number of parametrised stars in different quality regimes, (ii) the colour–effective temperature relation, (iii) an illustration of the T_{eff} spatial distribution, (iv) the atmospheric parameters of high-S/N spectra and associated constraints on stellar evolution models, and (v) the parametrisation of very metal-poor stars.

10.1. Number of parametrised stars in different quality regimes

As explained throughout this article, GSP-Spec has produced two sets of parameters (one from the MatisseGauguin workflow on the *AstrophysicalParameters* table, and another from the ANN workflow on the *AstrophysicalParametersSupp* table) for about 5.6 million stars from their RVS spectra. The total number of derived atmospheric parameters by both workflows and the number of GAUGUIN chemical abundances are illustrated in Fig. 17 (left panel for MatisseGauguin and right panel for ANN) and Fig. 18, respectively. In both figures, the total number of published parameters is shown together with the corresponding number for the best parametrised stars (from a high-quality selection, where all parameter flags are set to zero, including the abundance flags from MatisseGauguin). It is important to note that imposing that the full flag chain be equal to zero corresponds to very demanding requirements, including very low associated uncertainties. This selects about two million stars for the atmospheric parameters, whereas, for the chemical abundances (cf. Fig. 18), the number of estimates varies over several orders of magnitude from one element to another,

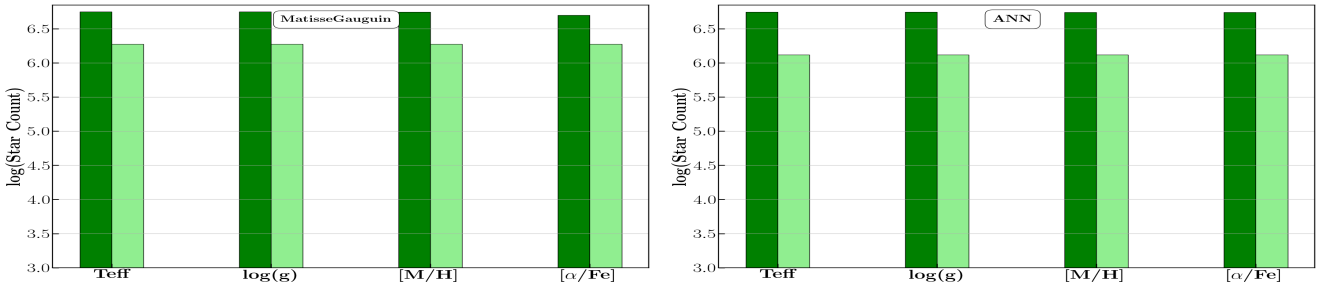

Fig. 17. Number of stars whose atmospheric parameters have been derived by MatisseGauguin and ANN (*left and right panels*, respectively). The dark green histograms refer to the whole sample whereas the light-green ones show only the very best parametrised stars with all their parameter quality flags equal to zero.

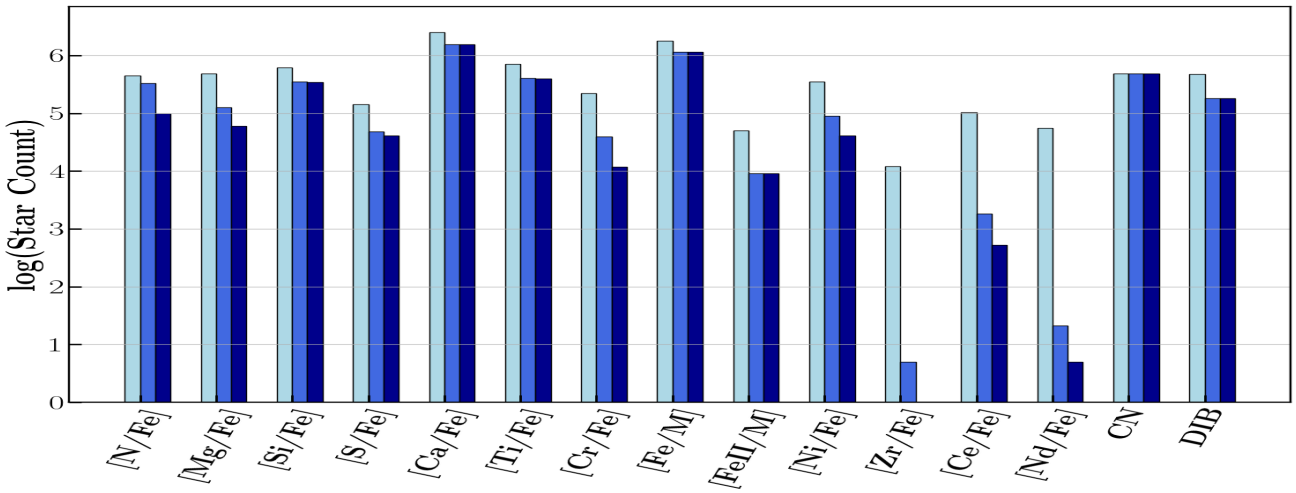

Fig. 18. Same as Fig. 17 but for the individual abundances derived by GAUGUIN plus the CN-abundance proxy and the DIB. The light-blue histogram (left bars) refers to the whole sample. The two other sets of bars (central and right bars) show only the very best stars with all their parameter flags and their abundance uncertainty quality equal to zero. The abundance upper limit flag is lower than or equal to one and equal to zero for the medium-blue and dark-blue bars, respectively.

as expected. In particular, calcium and iron (Fe I) are the most often derived species with estimates for around two millions stars, thanks to the Ca prominent lines and the numerous available iron lines. Abundances of heavy elements are derived for up to 10^4–10^5 stars, although these numbers strongly decrease when all the flags are used to filter (Ce being the heavy element with the highest number of estimates). However, we point out that this very strict quality filtering can be relaxed to increase number statistics, depending on the scientific goals of the user.

10.2. Colour–temperature relation

A classical way of validating effective temperature estimates is to verify their expected correlation with stellar colour. Figure 19 shows the trend between the (BP–RP) colour and the GSP-Spec $T_{\rm eff}$ estimates from MatisseGauguin. To consider the effect of extinction on the (BP–RP) colour, the points are colour coded according to the EW of the DIB derived for the same stars by GSP-Spec (only stars with the DIB flag equal to zero have been selected). First, it is observed that the lower envelope of the distribution corresponds to the lower DIB EW values, as expected from the correlation between DIB absorption and extinction. To quantify this observation, the median values of the distribution for the stars with a DIB EW lower than 0.05 Å (blue circles) can be compared to those whose DIB EW is equal to the median value of the distribution (0.07 Å for dwarf stars in the left panel, and 0.12 Å for giants in the right panel), plus a dispersion of ± 0.01 Å. Second, the observed relation is compared to a $T_{\rm eff}$ derived from the Casagrande et al. (2021) prescription (black dots) based on an implementation of *Gaia* and 2MASS photometry in the InfraRed Flux Method. No extinction has been considered in this case and the corresponding median values are shown as white circles. The Casagrande et al. (2021) predictions are in very good agreement with the low-extinction envelope of the GSP-Spec distribution (blue circles), validating the global behaviour of the estimated temperatures.

To complement this analysis, Fig. 20 presents the metallicty correlations of the colour–temperature relation for targets with all the parameter flags equal to zero. Again, the expected metallicty trend is observed in the low-extinction envelope. Interestingly, the higher extinction region above the lower envelope of the distribution is mainly occupied by metal-rich stars. This is expected from the fact that metal-rich stars are preferentially placed near the Galactic plane, where the interstellar extinction is higher.

10.3. Sky distribution of effective temperature estimates

Figure 21 presents the global all-sky spatial distribution in Galactic coordinates of the stars parametrised by GSP-Spec, colour-coded with their MatisseGauguin effective temperature